HAL open science

Fibre kinematics in dilute non-Newtonian fibre suspensions during confined and lubricated squeeze flow: direct numerical simulation and analytical modelling

Tanguy Laurencin, Patrice Laure, Laurent Orgeas, Pierre J.J. Dumont, Sabine Rolland Du Roscoat, Luisa Silva

To cite this version:

Tanguy Laurencin, Patrice Laure, Laurent Orgeas, Pierre J.J. Dumont, Sabine Rolland Du Roscoat, et al.. Fibre kinematics in dilute non-Newtonian fibre suspensions during confined and lubricated squeeze flow: direct numerical simulation and analytical modelling. Journal of Non-Newtonian Fluid Mechanics, 2019, 273, 10.1016/J.JNNFM.2019.104187 . hal-02320966

HAL Id: hal-02320966

https://hal.science/hal-02320966v1

Submitted on 20 Jul 2022

HAL is a multi-disciplinary open access archive for the deposit and dissemination of scientific research documents, whether they are published or not. The documents may come from teaching and research institutions in France or abroad, or from public or private research centers.

L'archive ouverte pluridisciplinaire **HAL**, est destinée au dépôt et à la diffusion de documents scientifiques de niveau recherche, publiés ou non, émanant des établissements d'enseignement et de recherche français ou étrangers, des laboratoires publics ou privés.

Distributed under a Creative Commons Attribution - NonCommercial 4.0 International License

Version of Record: https://www.sciencedirect.com/science/article/pii/S0377025718300296
Manuscript_6a6910bcb3e3c6fece5f04eff636dc1f

Fibre kinematics in dilute non-Newtonian fibre suspensions during confined and lubricated squeeze flow: direct numerical simulation and analytical modelling

T. Laurencin[a,b,c,d], P. Laure[b,e*], L. Orgéas[a],
P.J.J. Dumont[d], L. Silva[c], S. Rolland du Roscoat[a]

[a]Univ. Grenoble Alpes, CNRS, Grenoble INP, 3SR Lab, F-38000 Grenoble, France
[b]Univ. Côte d'Azur, CNRS, Lab. J.A. Dieudonné, Parc Valrose F-06000 Nice, France
[c]Ecole Centrale de Nantes, ICI, 1 rue de la Noë F-44000 Nantes, France
[d]Univ. Lyon, LaMCoS, INSA-Lyon, CNRS UMR5259, F-69621, Lyon, France
[e]PSL, CNRS, MINES ParisTech, CEMEF, 06904 Sophia Antipolis, France

Abstract
The properties of short fibre-reinforced polymer composites depend on the distribution and the orientation of fibres which drastically changes during the forming of composites. During this stage, these materials behave as fibre suspensions and usually flow in confined geometries. To analyse their flow-induced fibrous microstructures, we previously conducted 3D real-time *in situ* observations of the compression of non-Newtonian dilute fibre suspensions using fast X-ray microtomography [T. Laurencin et *al., Compos Sci Technol* **134** (2016)]. Here, we successfully simulated these experiments with a multi-domain Finite Element code and compared them with the predictions of Jeffery's model. Often, the Jeffery's equations agree with the experimental and numerical data. However, for fibres closed to compression platens, important deviations were observed with faster simulated and experimental fibre rotation. Adopting the dumbbell approach and revisiting the recent work of Perez *et al.* [*J non-Newtonian Fluid Mech* **233** (2016)], an extension of the Jeffery's model is proposed to account both for the non-Newtonian rheology of the suspending fluid and confinement effects. Despite its simplicity, the new model allows a good description of simulation and experimental results.

Keywords: Short fibre-reinforced composites; Fibre suspension; Direct numerical simulation; Confinement; Jeffery's model.

1. Introduction

Knowing the distribution and the orientation in short fibre-reinforced polymer (nano)composites is essential to control their physical and mechanical properties [1-3, 57]. These materials have fibre volume fractions ϕ that range from 0.005 to 0.5 and fibre aspect ratios $\beta = l/d$ from 5 to 1000 (d and l being the typical fibre diameter and length). During the forming stages, they behave as fibre suspensions with a complex rheology (in particular due to the non-Newtonian behaviour of the polymer matrices) and drastic flow-induced changes of the distribution and the orientation of fibres. In practice, the suspension usually flows occur in confined regions where the typical size h is of the same order of magnitude as the size of the fibre length l, *i.e*, with a confinement parameter $C^* = h/l = \mathcal{O}(1)$ [4-6]. These confined

* Corresponding author's email : patrice.laure@unice.fr

© 2019 published by Elsevier. This manuscript is made available under the CC BY NC user license
https://creativecommons.org/licenses/by-nc/4.0/

flow situations conduct to interactions between fibres and solid boundaries that alter the fibre kinematics. These effects should be considered to simulate the processing of short fibre-reinforced polymer composites but are still not very well-understood or modelled, due to numerical or experimental difficulties to properly observe the evolving fibrous microstructures and to access to flow mechanisms at fibre scale.

Fibre kinematics under various flow have been widely studied starting from the fundamental work of Jeffery [7] focused on the motion of an ellipsoidal particle immersed in an incompressible Newtonian fluid flowing at low Reynolds number in an infinite domain. The theory assumes that the translation of the considered particle is an affine function of the macroscale velocity gradient. In the case of a cylindrical fibre, the evolution of the unit tangent vector $\mathbf{p} = sin\theta\ cos\varphi\ \mathbf{e}_1 + sin\theta\ sin\varphi\ \mathbf{e}_2\ + cos\theta\mathbf{e}_3$, characterising the fibre orientation, can be predicted from its rate $\dot{\mathbf{p}}$, the macroscale vorticity tensor $\mathbf{\Omega}$ and the strain rate tensor $\mathbf{D}$:

$$\dot{\mathbf{p}} = \mathbf{\Omega}.\mathbf{p} + \lambda(\mathbf{D}.\mathbf{p}\ - (\mathbf{p}.\mathbf{D}.\mathbf{p})\mathbf{p}) \quad \text{with} \quad \lambda = 1 - \frac{16.35\ln\beta}{4\pi\beta^2} \qquad \text{Eq. (1)}$$

where λ is a shape factor expressed by Brenner for cylindrical fibres [8]. The relevance of Jeffery's model was experimentally confirmed by several authors [9-12], mostly under shear flow. Jeffery's model has largely been validated and used for dilute Newtonian fibre suspensions, *i.e.*, when $\phi \ll 1/\beta^2$ [13-15]. The model was also enriched for semi-dilute and Newtonian fibre suspensions $(1/\beta^2 \ll \phi \ll 1/\beta)$ to take into account for long range hydrodynamic fibre interactions [16-20]. In these approaches, the motions of the centres of mass of fibres are still affine functions of the macroscale velocity gradients and the fibre rotations are restrained thanks to a diffusion-like term depending on the Fibre Orientation Distribution Function (FODF) added in the right hand-side of Eq. (1). In the concentrated regime, the as-modified Jeffery's model fails due to short range interactions between fibres which play a central role on rheological behaviour of these suspensions [16, 21-23].

The effects of the non-Newtonian rheology of the suspending fluid on the kinematics of single ellipsoidal particle under simple shear flow have been studied only by a few authors [24-30,

59]. For sheared viscoelastic fluids, experimental observations revealed a departure from Jeffery's orbits with a bistability of particle orientation which depends on the elasticity of the fluid. At low Deborah number, fibre aligns along the vorticity direction [24-29], whereas increasing the Deborah number leads to an orientation transition to the shear direction [27, 28, and 30]. Theoretical studies using second order suspending fluids in the limit of low Weissenberg number were also developed by Leal [31] for the motion of rod with a Rivlin-Ericksen fluid model, and Brunn [32] for the motion of transversely isotropic particle with a Giesekus fluid model. Also, Borzacchiello *et al.* [33] developed a simplified model by enriching the velocity gradient with a first-order perturbation induced by the particle and the non-Newtonian fluid (Giesekus fluid model in the limit of low Weissenberg number). Qualitatively, the predictions of the model are in agreement with experimental observations [29] and direct numerical simulations [34]. However, very few experimental, theoretical, and numerical studies focused on the strain-thinning behaviour of the suspending fluid under compressive or elongational flow [15, 21] despite these features are commonly encountered in the processing of short fibre-reinforced polymer composites.

The aforementioned theories were established for a good scale separation, *i.e.*, when $C^* \gg 1$. Confinement effects occurring when $C^* = \mathcal{O}(1)$ have been much less analysed. Departures from Jeffery's trajectories and orbits were reported for fibres that interacted with mould walls in Newtonian [35-38] as well as non-Newtonian suspending fluids [39]. Various complex kinematics were observed such as "glancing" [38], "pole vaulting" [39] or "stabilizing effect" [37]. The influence on confinement on rheology of fiber suspensions is also studied for shear and elongational flows [57, 58]. To the best of the authors' knowledge, only a few authors modelled these effects. Using the heuristic dumbbell model, modifications of the Jeffery's equations [57, 40-42] were proposed by considering physical contacts between rods and walls through the introduction of a contact force ensuring wall impenetrability. However, confinement effects have rarely been studied in the case of non-Newtonian suspending fluids [39], and never for elongational flows.

Within this context, we recently used real time and *in situ* synchrotron X-ray microtomography to finely assess the 3D fibre kinematics in dilute suspensions with a strain-thinning fluid during confined and lubricated compression [43]. Results showed that power-law index and confinement had minor effects on fibre kinematics only if the fibre/fibre and fibre/wall distances remained sufficiently large (approximately above twice the fibre diameter). Below, fibres exhibited noticeable departures from Jeffery's predictions. In this paper, we model these experiments using both direct fibre scale numerical simulation and analytical predictions. Thus, after briefly recalling the used numerical approach, we extend the analytical dumbbell approach to model fibre kinematics in (un)confined flows [41, 42, 44 and 45] for power law fluids. Experiments that have motivated this work are briefly summarized. Theoretical, experimental and numerical results are then compared and discussed.

2. Fibre suspensions in lubricated squeeze flow: Methods

2.1 Numerical approach

2.1.1 Boundary values problem to be solved

We considered a cubic domain Ω composed of subdomains Ω_j made of N fibres i, the suspending fluid f, the air a and the compression platens p (Figure 1). Fibre suspensions were modelled as cylindrical samples (height h and radius R) and located between two parallel rigid compression platens (die and punch). Each fibre i with an orientation vector $\mathbf{p}_i$ and a centre of mass G_i located at a position $\mathbf{x}_{G_i}$ was placed inside the suspending fluid. Compression flow was imposed with a zero stress vector on the external boundaries of the domain Ω and with the motion of the upper platen at a velocity $\mathbf{v}(x, y, h) = (0,0,\dot{h})$ at a prescribed compression strain rate $D_{33} = \dot{h}/h$.

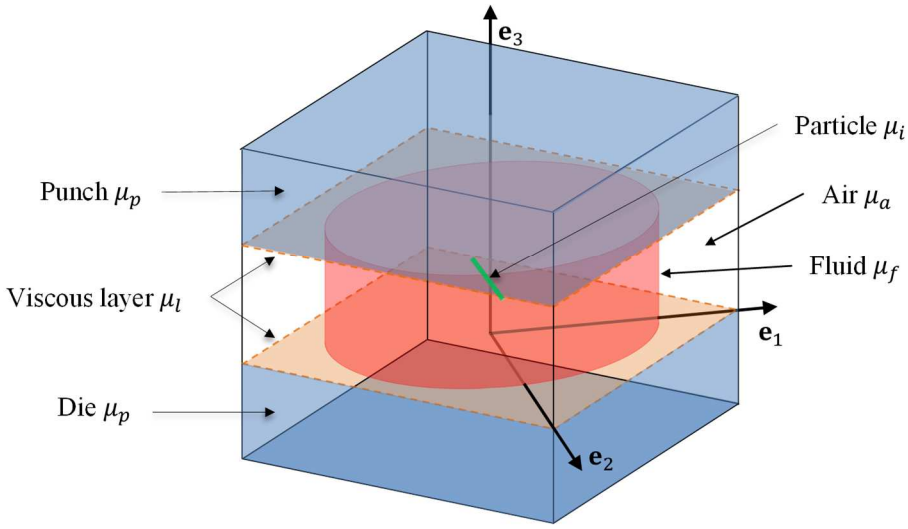

Figure 1. Multi-domain approach used with the immersed domain method to simulate the lubricated squeeze flow: subdomains used to describe axisymmetric squeeze flows; each domain was assumed to be incompressible viscous body.

All the phases, namely the platens, the air, the suspending fluid, the fibre and the viscous layers were assumed to behave as incompressible power-law fluids with proper viscosities μ_j and kinematic constraints. By neglecting inertia effects, the overall motion in Ω was ruled by the following momentum and mass balance equations:

$$\begin{cases} \boldsymbol{\nabla} \cdot 2\mu\mathbf{D} - \boldsymbol{\nabla}p = \mathbf{0} \\ \boldsymbol{\nabla} \cdot \mathbf{v} = 0 \end{cases} \quad \text{in } \Omega. \qquad \text{Eq. (2)}$$

where μ is the viscosity function in Ω, p the incompressibility pressure and $\mathbf{v}$ the velocity field. The proposed monolithic formulation consists in finding $\mathbf{v}$ and p all over the global domain Ω. To close the boundary values problem, the following constitutive equations were made:

- In the suspending fluid Ω_f, the fluid viscosity μ_f was assumed to follow a power law, *i.e.*, $\mu_f = k\dot{\gamma}_{eq}{}^{n-1}$; $n \leq 1$, where k was the consistency, n the power-law index and $\dot{\gamma}_{eq} = \sqrt{2\mathbf{D}:\mathbf{D}}$ the generalised shear rate.
- Fibres were considered as rigid bodies. Thus, in the fibre sub-domains Ω_i, the viscosities μ_i were set to a large constant value and an extra term $\boldsymbol{\nabla} \cdot \boldsymbol{\sigma}^*$ was added on the right-hand side of the momentum equation Eq. (2) where the stress tensor $\boldsymbol{\sigma}^*$ is a Lagrange multiplier linked to the rigidity constraint $\mathbf{D} = \mathbf{0}$ [46]. Thus, after convergence, the first term in Eq. (2) vanished, μ_i only playing the role of a penalisation factor.

- The air and mould viscosities were set to constant values and were adjusted at each time step with respect to the fluid viscosity μ_f in order to get a plug flow for the suspension, *i.e.*, a cylindrical front at the air/fluid interface. Using preliminary simulations, we found that the air viscosity μ_a could be purposely fixed to $10^{-3}\min(\mu_f)$, whereas the solid motion inside the mould could be properly recovered if the platen viscosity μ_p was around $10^3\max(\mu_f)$. Thin lubricated layers having the same thickness as the size of mixing layer defined further were also added at the platen/fluid interfaces in order to get a plug flow corresponding to perfect slip boundary conditions [47]. For that purpose, preliminary simulations allowed us to adjust the constant viscosity μ_l to the same value as the air viscosity μ_a.

2.1.2 Numerical schemes

From a numerical viewpoint, the momentum equation Eq. (2) was computed in Ω with a finite element method. All subdomains were embedded in a unique Eulerian mesh using the immersed volume method [46]. Thus, level-sets were used to get (i) implicit representation of interfaces between subdomains and (ii) proper definition of the viscosity μ as a space dependent function [46, 48]. Each level set α_j was associated with a sub-domain Ω_j. Except for the air levelset α_a that was defined as the complementary of all the other ones, a levelset α_j representing a positive/negative distance to the subdomain interface Γ_j was introduced:

$$\alpha_j = \begin{cases} +d_j(\mathbf{x}) & \text{if } \mathbf{x} \in \Omega_j \\ -d_j(\mathbf{x}) & \text{if } \mathbf{x} \notin \Omega_j \end{cases}. \qquad \text{Eq. (3)}$$

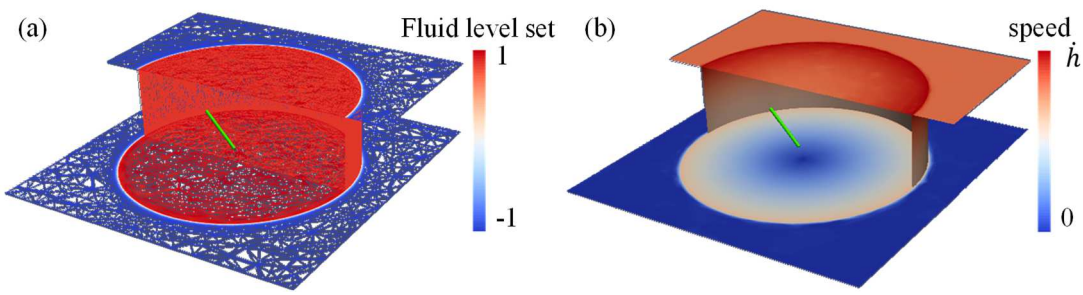

Figure 2. (a) Iso-values of the truncated fluid level-set φ_f and adaptive mesh used to run the simulation, displayed on platens and fluid domains. (b) Iso-values of the velocity magnitude shown on platens and fluid domains.

Level set functions enabled us to properly ascribe the overall viscosity μ to its value μ_j in sub-domains Ω_j. This was achieved by using smooth Heaviside functions H_j :

$$\mu(\mathbf{x}) = \sum_j H_j(\mathbf{x})\ \mu_j + \left(1 - \sum_j H_j(\mathbf{x})\right) \mu_a. \qquad \text{Eq. (4)}$$

Practically, levelsets were truncated in a narrow interval $[-e, e]$ using hyperbolic filters $\varphi_j = e \tanh(\alpha_j / e)$ (Fig. 2a). Moreover, the functions H_j also depended on e, *i.e.*, $H_j = 1/2\left(1 + \varphi_j / e\right)$ in order to ensure smooth transitions of μ between subdomains.

Within this framework, the velocity and the pressure fields were computed by solving momentum and continuity equations (Eq. (2)), as illustrated in Fig. 2b. The corresponding weak formulation was solved using the augmented Lagrangian method and the Uzawa algorithm [49] with mixed finite elements MINI-elements (P1+/P1) [50]. In addition, at a given time step, once the velocity field was estimated, the levelset positions in Ω could be updated:

- Levelsets of compression platens were updated from their given rigid body kinematics.
- Thanks to an efficient algorithm used to interpolate the velocity and vorticity at the centre of fibres [51], the positions $\mathbf{x}_i$ and the orientations $\mathbf{p}_i$ of the N fibres were updated by integrating the following motion equations:

$$\begin{cases} \frac{d\mathbf{x}_i}{dt} = \mathbf{v}(\mathbf{x}_i) \\ \frac{d\mathbf{p}_i}{dt} = \frac{1}{2}\boldsymbol{\nabla} \times \mathbf{v}(\mathbf{x}_i) \cdot \mathbf{p}_i \end{cases}. \qquad \text{Eq. (5)}$$

This was done using a second order Adams-Bashforth scheme. Once the new positions and orientations of the particles were determined, their shapes were updated.

- The truncated levelset associated to the fluid/air interface was transported by the velocity solution $\mathbf{v}$ of the monolithic system according to the following sets of equations:

$$\begin{cases} \frac{\partial \varphi_f}{\partial t} + \mathbf{v} \,.\, \boldsymbol{\nabla}\varphi_f = 0 \\ \varphi_f(t = 0, \mathbf{x}) = \varphi_{f0}(\mathbf{x}) \end{cases}. \qquad \text{Eq. (6)}$$

A re-initialization step was also proven to be necessary to maintain the geometrical properties of this levelset [46]. Thus, giving the evolution of the air/fluid interface, Eq. (6) was slightly modified as explained in Ville and *al.* [52].

Finally, to solve the above set of equations, optimal meshes were generated using an anisotropic mesh adaptation based on an *a posteriori* interpolation error [46, 53]. This meshing procedure enabled to capture high gradients of the flow solution with a good accuracy at a very low number of elements. The building of unstructured anisotropic meshes was based on local mesh modifications, using a metric which minimised the errors on multiple fields (namely the velocity and the levelset functions associated to the platens, particles and the fluid). In order to concentrate the mesh in the neighbourhood of the different interfaces, the levelset functions were replaced by their tangentially filtered functions with a characteristic thickness $E = 5\,e$ (e being the characteristic thickness used for mixing law). An example of anisotropic mesh is plotted in Fig. 2a. Our computations were made on a unitary cube Ω (the equations were scaled with a reference length) with $e = 10^{-3}$. The number of nodes ranged from 80 000 to 250 000 according to the number of fibres, the time step being equal to $0.5\,10^{-3}$ (scaled time). For the most suspensions, the calculation time for a compression test was around two days on twenty processors until a Hencky compression strain $|\varepsilon_{33}| = 0.8$.

2.2 Theoretical approach

As mentioned in the introduction, a few authors modelled confinement effects and in particular the collision between fibres and walls during the suspension flows. Recently, Perez *et al.* [41] proposed a direct modification of Jeffery's model in the case of slender cylindrical fibres ($\lambda = 1$) immersed in an incompressible Newtonian fluid submitted to simple shear flow in symmetrical contacts with walls. The analysis is based on the rigid dumbbell model introduced by Bird *et al.* [44] and was recently extended to non-symmetrical contacts, Poiseuille and squeeze flows [6]. Herein, we revisit and extend it to the case of dilute fibre suspensions with power law fluids, with a proper description of contact conditions in confined situations.

Hence, each fibre i of the suspension is idealised as a dumbbell of unit orientation vector $\mathbf{p}_i$, centre of mass G_i of position $\mathbf{x}_{G_i}$ and velocity field $\mathbf{v}_{G_i}$ and with two beads of diameter d

separated by a distance l (Figure 3). The upper (+) and the lower (−) beads have respective positions $\mathbf{x}_i^{\pm}$ and velocities:

$$\mathbf{v}_i^{\pm} = \mathbf{v}_{G_i} \pm \frac{l}{2}\dot{\mathbf{p}}_i \,. \qquad \text{Eq. (7)}$$

During the suspension flow, the dumbbell is subjected to hydrodynamic forces which were further denoted $\mathbf{f}_i^{h^{\pm}}$, and exerted on the upper and lower beads. These forces are assumed to depend on the relative velocity $\Delta\mathbf{v}_i^{\pm}$ between the fluid and the beads:

$$\Delta\mathbf{v}_i^{\pm} = \mathbf{V}_{G_i} \pm \frac{l}{2}\nabla\mathbf{V}\cdot\mathbf{p}_i - \mathbf{v}_i^{\pm} \,, \qquad \text{Eq. (8)}$$

where $\nabla\mathbf{V}$ is the macroscale velocity gradient and where $\mathbf{V}_{G_i}$ is the velocity of the fluid surrounding the dumbbell at its centre of mass G_i.

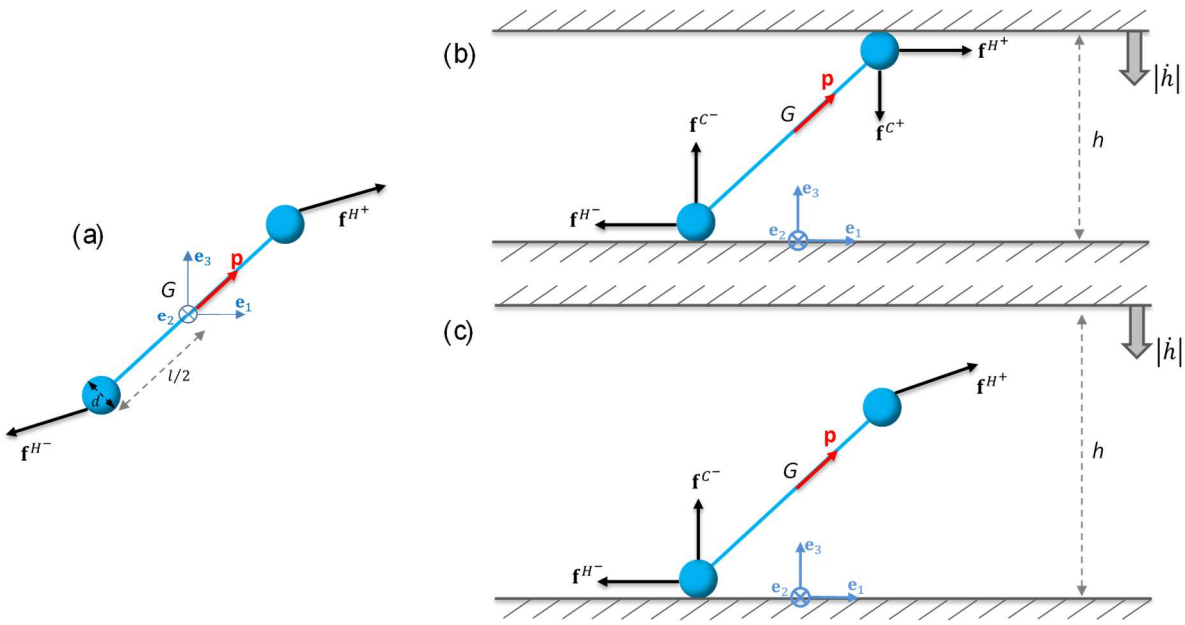

Figure 3. Fiber i modeled by a dumbbell. (a) Unconfined lubricated squeeze flow with hydrodynamic forces $\mathbf{f}_i^{h^{\pm}}$ exerted on the upper and lower beads. (b) Confined lubricated squeeze flow with centred dumbbell, hydrodynamic $\mathbf{f}_i^{h^{\pm}}$ and contact $\mathbf{f}_i^{c^{\pm}}$ forces exerted on the upper and lower beads. (c) Confined lubricated squeeze flow with only one contact with the lower wall.

By analogy with the expressions proposed by Bruschke and Advani [54] and Spelt *et al.* [55] for power-law fluids, or more generally by Orgéas *et al.* [56] for power law fluids, the hydrodynamic force $\mathbf{f}_i^{h}$ is assumed to be the gradient of a convex viscous dissipation potential $\mathbf{\Phi}^{h}(\mathbf{\Delta v})$ with respect to the relative velocity $\mathbf{\Delta v}_i$ between the dumbbell and the fluid at the considered point:

$$\mathbf{f}_i^h = \frac{\partial \Phi^h}{\partial \Delta \mathbf{v}_i}, \qquad \text{Eq. (9)}$$

and such that

$$\mathbf{f}_i^h(-\Delta \mathbf{v}_i) = -\mathbf{f}_i^h(\Delta \mathbf{v}_i). \qquad \text{Eq. (10)}$$

The convexity of Φ^h ensures that

$$\mathbf{f}_i^h(\Delta \mathbf{v}_i) = \mathbf{f}_i^h\left(\Delta \mathbf{v}_i^{'}\right) \quad \Leftrightarrow \quad \Delta \mathbf{v}_i^{'} = \Delta \mathbf{v}_i. \qquad \text{Eq. (11)}$$

The potential Φ^h is expressed as a function of a norm $\Delta v_{eqi}(\Delta \mathbf{v}_i)$ of the relative velocity $\Delta \mathbf{v}_i$ [56]:

$$\mathbf{f}_i^h = \frac{\partial \Phi^h}{\partial \Delta v_{eqi}} \frac{\partial \Delta v_{eqi}}{\partial \Delta \mathbf{v}_i} = \xi \frac{\partial \Delta v_{eqi}}{\partial \Delta \mathbf{v}_i}, \qquad \text{Eq. (12)}$$

where the hydrodynamic drag coefficient ξ is a positive and convex rheological function of Δv_{eqi}. For example, if $\Delta v_{eqi} = \|\Delta \mathbf{v}_i\|$ (as in [41, 42]), Eq. (12) writes as follows:

$$\mathbf{f}_i^h = \xi_i \Delta \mathbf{v}_i. \qquad \text{Eq. (13)}$$

For power-law fluids (as considered in this study), the drag coefficient ξ_i can be expressed as:

$$\xi_i = \xi_0 \Delta v_{eqi}^{n-1}, \qquad \text{Eq. (14)}$$

where ξ_0 is a constant and n the power-law index of the suspending fluid.

2.2.1 Unconfined lubricated squeeze flows

If the dilute fibre suspensions are squeezed with unconfined and quasi-static flow situations, the first momentum balance equation of the dumbbell i yields:

$$\mathbf{f}_i^{h^-} = -\mathbf{f}_i^{h^+} \qquad \text{Eq. (15)}$$

According to Eqs. (9-14), and taking into account the expressions of the upper and lower relative velocities Eqs. (7-8), the following result was straightforwardly obtained:

$$\mathbf{v}_{G_i} = \mathbf{V}_{G_i} \qquad \text{Eq. (16)}$$

Thus, as for the Newtonian and isotropic case [41], the translation of the dumbbell in a power law fluid follows that of the suspending fluid. In addition, the resulting torque at the centre of the dumbbell is null. Therefore the forces that act on each bead are colinear with the orientation vector $\mathbf{p}_i$:

$$\mathbf{f}_i^{h^+} = \alpha \mathbf{p}_i \;\Leftrightarrow\; \xi_i^+ \left(\frac{l}{2}\nabla\mathbf{V}\cdot\mathbf{p}_i - \frac{l}{2}\dot{\mathbf{p}}_i\right) = \alpha\mathbf{p}_i\,, \qquad \text{Eq. (17)}$$

where $\xi_i^+ = \xi_i\big(\Delta v_{eqi}(\Delta\mathbf{v}_i^+)\big)$. Multiplying the last equation by $\mathbf{p}_i$ and accounting for $\mathbf{p}_i\cdot\mathbf{p}_i = 1$, and thus for $\mathbf{p}_i\cdot\dot{\mathbf{p}}_i = 0$, we obtain:

$$\alpha = \xi_i^+ \left(\frac{l}{2}\nabla\mathbf{V}\colon \mathbf{p}_i\otimes\mathbf{p}_i\right), \qquad \text{Eq. (18)}$$

Replacing the expression of α in Eq. (17) gives:

$$\dot{\mathbf{p}}_i = \dot{\mathbf{p}}_i^J = \nabla\mathbf{V}\cdot\mathbf{p}_i - (\nabla\mathbf{V}\colon\mathbf{p}_i\otimes\mathbf{p}_i)\mathbf{p}_i\,. \qquad \text{Eq. (19)}$$

Hence, regardless of the considered power law suspending fluids, the rotary velocity $\dot{\mathbf{p}}_i$ of the dumbbell is equivalent to that given by the Jeffery's model $\dot{\mathbf{p}}_i^J$ (with $\lambda = 1$).

2.2.2 Confined lubricated squeeze flows: centred fibres

We now consider the case where the dumbbell i is confined and centred between two parallel compression platens ($C^* = \mathcal{O}(1)$). If its beads do not touch the platens and neglecting lubrication forces normal to the compression platens as the beads become close to them, the problem is identical to the previous unconfined flow situation: $\mathbf{v}_{G_i}$ is an affine function of $\nabla\mathbf{V}$ and $\dot{\mathbf{p}}_i = \dot{\mathbf{p}}_i^J$. The problem has to be reconsidered when symmetrical contacts occur between the dumbbell and the walls (Figure 3b), *i.e.*, when $\mathbf{x}_i^-\cdot\mathbf{e}_3 = d/2$. Then two flow situations occur. The first one corresponds to $\dot{h} \geq 0$. For this flow configuration (uniaxial tensile flow), one recovers again the unconfined situation, *i.e.*, $\mathbf{v}_{G_i} = \mathbf{V}_{G_i}$ and $\dot{\mathbf{p}}_i = \dot{\mathbf{p}}_i^J$. The second case occurs when $\dot{h} < 0$ (uniaxial compression). Here, opposite contact forces $\mathbf{f}_i^{c^+}$ and $\mathbf{f}_i^{c^-}$ are introduced [41]. They are exerted along the direction perpendicular to the upper and the lower walls, *i.e.,* the direction $\mathbf{e}_3$ in this study:

$$\mathbf{f}_i^{c^\pm} = \mp f_i^c\mathbf{e}_3. \qquad \text{Eq. (20)}$$

where f_i^c is the norm of the contact forces. The first momentum balance equation projected along the compression platens also yields Eq. (15). Taking into account the force properties of Eqs. (10-11) finally yields Eq. (16) so that the dumbbell translation follows that of the suspending fluid. Furthermore, as the overall torque at the centre of the dumbbell has to vanish, forces exerted at the beads are collinear with the dumbbell orientation vector $\mathbf{p}_i$:

$$\mathbf{f}_i^{h^+} + \mathbf{f}_i^{c^+} = \alpha' \mathbf{p}_i \qquad \text{Eq. (21)}$$

Multiplying the last equation by the unit orientation vector $\mathbf{p}_i$ and keeping in mind that $\mathbf{p}_i \cdot \dot{\mathbf{p}}_i = 0$, an expression of the scalar α' can be obtained so that Eq. (21) yields the following expression of the rotary velocity of the dumbbell:

$$\dot{\mathbf{p}}_i = \dot{\mathbf{p}}_i^J + \dot{\mathbf{p}}_i^c = \nabla\mathbf{V} \cdot \mathbf{p}_i - (\nabla\mathbf{V} : \mathbf{p}_i \otimes \mathbf{p}_i)\mathbf{p}_i + \frac{2f_i^c}{l\xi_i^+}(p_{i3}\mathbf{p}_i - \mathbf{e}_3) \qquad \text{Eq. (22)}$$

with p_{i3} the component of the dumbbell orientation vector along $\mathbf{e}_3$**.** Using the affine result, the last expression as well as the non-penetration conditions of the beads at the walls, *e.g.*, $\mathbf{v}_i^- \cdot \mathbf{e}_3 = 0$ for the lower bead, leads to:

$$\frac{2f_i^c}{l\xi_i^+} = \frac{\dot{p}_{i3}^J - D_{33}^d p_{i3}}{1 - p_{i3}^2} \qquad \text{Eq. (23)}$$

where $D_{33}^d = D_{33}\,(1 + 1/\beta\, p_3)$. This yields the following expression of the contact contribution $\dot{\mathbf{p}}_i^c$ of rotary velocity of the dumbbell:

$$\dot{\mathbf{p}}_i^c = \frac{\dot{p}_{i3}^J - D_{33}^d\, p_{i3}}{1 - p_{i3}^2}\left(p_{i3}\mathbf{p}_i - \mathbf{e}_3\right) \qquad \text{Eq. (24)}$$

More precisely the rotation rate of the third component (namely the out-of-plane angle θ) reads

$$\dot{p}_{i3}^c = -\,\dot{p}_{i3}^J\,\frac{1 - 3\,p_{i3}^2 - 2/\beta\, p_{i3}}{3\left(1 - p_{i3}^2\right)} \qquad \text{Eq. (25)}$$

The sign of numerator, $1 - 3\,p_{i3}^2 - 2/\beta\, p_{i3}$, gives the evolution of the rotation rate (either a faster or a slower rotation). For large aspect ratio β, the change of sign occurs around $55°$. Basic numerical computations show that this angle increases for small value of β.

In conclusion for this elongational flow, the translation of the dumbbell centre of mass is still an affine function of the macroscale fluid velocity. In addition, if the contact condition is fulfilled and the contact contribution Eq. (25) becomes effective, the fibre rotation rate is higher than that predicted by the Jeffery's model for fiber having an out-of-plane angle lower than $55°$. On the other hand, the effect of contact between platen and fiber is less important

for fiber already aligned with horizontal platens. It is important to mention that these results do not depend on the rheology of the considered suspending fluids.

2.2.3 Confined lubricated squeeze flows: non-centred fibres

Lastly, we consider the case where the dumbbell i is positioned asymmetrically with respect to the walls, *i.e.*, with its centre of mass G_i closer to one wall, *e.g.* the lower platen as shown in Figure 3c. Here again, as long as the dumbbell does not touch the platens, the dumbbell kinematics is the same as in the unconfined case. When $\mathbf{x}_i^- \cdot \mathbf{e}_3 = d/2$, the dumbbell touches the lower compression platen and its kinematics is that of the unconfined case if $\dot{h} \geq 0$. The contact force $\mathbf{f}_i^{c^-}$ is exerted on the lower bead when $\dot{h} < 0$. The first momentum balance then yields:

$$\mathbf{f}_i^{h^-} + \mathbf{f}_i^{c^-} + \mathbf{f}_i^{h^+} = \mathbf{0}, \qquad \text{Eq. (26)}$$

leading to the following expression of $\mathbf{v}_{G_i} - \mathbf{V}_{G_i}$:

$$\mathbf{v}_{G_i} - \mathbf{V}_{G_i} = \frac{l}{2}\,\frac{\xi_i^+ - \xi_i^-}{\xi_i^+ + \xi_i^-}(\boldsymbol{\nabla}\mathbf{V} \cdot \mathbf{p}_i - \dot{\mathbf{p}}_i) + \frac{f_i^c}{\xi_i^+ + \xi_i^-}\mathbf{e}_3 \qquad \text{Eq. (27)}$$

To simplify this expression, we temporarily consider the same problem, but with the dumbbell touching the upper platen instead of the lower one (denoted with the symbol "$*$" in the following). The similarity of the problem with respect to that sketched in Figure 3c is such that the orientation $\mathbf{p}_i^*$ and the orientation rate $\dot{\mathbf{p}}_i^*$ of the dumbbell, the contact force intensity f_i^{c*} as well as the function $\xi_i^{+*} + \xi_i^{-*}$ must be identical. Therefore, one easily gets:

$$\mathbf{v}_{G_i}^* - \mathbf{V}_{G_i}^* = \frac{l}{2}\,\frac{\xi_i^{+*} - \xi_i^{-*}}{\xi_i^{+*} + \xi_i^{-*}}(\boldsymbol{\nabla}\mathbf{V} \cdot \mathbf{p}_i - \dot{\mathbf{p}}_i) - \frac{f_i^c}{\xi_i^{+*} + \xi_i^{-*}}\mathbf{e}_3 \qquad \text{Eq. (28)}$$

In addition, the vertical fluctuations $(\mathbf{v}_{G_i} - \mathbf{V}_{G_i}) \cdot \mathbf{e}_3$ and $(\mathbf{v}_{G_i}^* - \mathbf{V}_{G_i}^*) \cdot \mathbf{e}_3$ must be opposite. Hence, accounting for the two last equations, this condition is fulfilled when $\xi_i^+ = \xi_i^-$ (or $\xi_i^{+*} = \xi_i^{-*}$). Consequently, for the flow situation considered in Figure 3c, the following expression is obtained:

$$\mathbf{v}_{G_i} = \mathbf{V}_{G_i} + \frac{f_i^c}{2\xi_i^-}\mathbf{e}_3 \qquad \text{Eq. (29)}$$

where the vertical fluid velocity $V_{G_{i3}}$ at the center of mass is equal to $(l/2\, p_3 + d/2)\, \dot{h}/h$. The second momentum balance implies that the forces exerted on each bead must be colinear. For the upper beads this is expressed as:

$$\mathbf{f}_i^{h^+} = \alpha'' \mathbf{p}_i, \qquad \text{Eq. (30)}$$

As before, this leads to the following expression of the rotary velocity of the dumbbell:

$$\dot{\mathbf{p}}_i = \dot{\mathbf{p}}_i^J + \dot{\mathbf{p}}_i^c = \nabla \mathbf{V} \cdot \mathbf{p}_i - (\nabla \mathbf{V} : \mathbf{p}_i \otimes \mathbf{p}_i)\mathbf{p}_i + \frac{f_i^c}{l\xi_i^-}(p_{i3}\mathbf{p}_i - \mathbf{e}_3). \qquad \text{Eq. (31)}$$

Combined with the non-penetration condition $\mathbf{v}_i^- \cdot \mathbf{e}_3 = 0$ for the lower bead, this leads to:

$$\dot{\mathbf{p}}_i^c = \frac{\dot{p}_{i3}^J - D_{33}^d\, p_{i3}}{2 - p_{i3}^2}(p_{i3}\mathbf{p}_i - \mathbf{e}_3) \qquad \text{Eq. (32)}$$

As in the previous section, the third component expresses the rotation rate,

$$\dot{p}_{i3}^c = -\, \dot{p}_{i3}^J\, \frac{1 - 3\, p_{i3}^2 - 2/\beta\, p_{i3}}{3\,(2 - p_{i3}^2)} \qquad \text{Eq. (33)}$$

where only the denominator changes with respect to Eq. (25).

With the non-penetration condition, an expression of $\mathbf{v}_{G_i}$ can also be obtained:

$$\mathbf{v}_{G_i} = \mathbf{V}_{G_i} + \frac{l}{2}\frac{\dot{p}_{i3}^J - D_{33}\left(p_{i3} + \frac{1}{\beta}\right)}{2 - p_{i3}^2}\mathbf{e}_3 \qquad \text{Eq. (34)}$$

Consequently, for asymmetrical configurations, if the contact condition is fulfilled and if the compression platens become closer, the two last equations prove that (i) the translation of the dumbbell centre of mass is no more an affine function of the macroscale fluid velocity, (ii) as in the previous section, the fibre rotation rate is higher than that predicted by the Jeffery's model when the vertical angle is lower than $55°$. Here again, it is interesting to notice that these results do not depend on the rheology of the considered suspending fluids.

2.3 Experimental approach

We briefly recall here the information related to the experiment that have been reported in [43], the results which will be compared to the numerical simulation in the next section. Non-Newtonian dilute fibre suspensions were prepared and subjected to lubricated compression experiments using a micro-rheometer mounted in a synchrotron X-ray microtomograph

(Tomcat beamline, SLS, Villigen, Switzerland). The fluid used to make fibre suspensions was a hydrocarbon gel (paraffin). At $50°C$, the gel viscosity exhibited a non-Newtonian strain-thinning power-law close to that of polymer matrices used in the composite industry, with a consistency $k = 440\ Pa.s^{1-n}$ and a power-law index $n = 0.2$. Fibres were extracted from fluorocarbon (PVDF) elastic fishing wire (diameter $d = 200\ \mu m$). More details about the matrix rheology or the suspension processing are reported in [43]. Fibre suspensions were subjected to lubricated simple compression loading at $50°C$ and constant velocities $\dot{h}$. The suspension flow was considered as confined due to poor scale separation such that $C^* = h/l = \mathcal{O}(1)$. The 3D fibrous microstructures and the flow fronts of the suspensions were imaged in real-time using fast X-ray microtomography. Nine experiments were performed: six samples with one fibre placed in the centre of samples and different initial orientations $(\theta_i^0, \varphi_i^0)$, and three samples with five to eight fibres corresponding to a dilute concentration regime ($\phi \ll 1/\beta^2$), as summarised in Tab. 1.

$Test\ number$	1	2	3	4	5	6	7	8	9
N	1	1	1	1	1	1	5	8	8
ϕ (%)	0.013	0.013	0.015	0.013	0.011	0.011	0.11	0.21	0.16
β	16.5	17	19.5	17.5	14.5	14.5	12.6	17.9	17.7
$D_{33}^0 (s^{-1})$	0.004	0.004	0.03	0.03	0.03	0.03	0.03	0.004	0.03
$\Delta x_{min}^{Exp}(\%)$	-	-	-	-	-	-	2.0	2.1	1.5
$\Delta x_{max}^{Exp}(\%)$	8	7.5	8.2	5.6	7.6	3.9	4.1	7.1	5.9
$\Delta x_{min}^{Num}(\%)$	-	-	-	-	-	-	0.5	0.5	0.3
$\Delta x_{max}^{Num}(\%)$	0.6	0.3	0.15	0.6	0.2	0.7	1.4	3	2.1

Table 1. – Test number with their characteristics: number of fibres N and fibre aspect ratio β in the suspensions, initial strain rate D_{33}^0 used for the compression test, minimal Δx_{min}^i and maximal Δx_{max}^i recorded dispersion for the position of the fibre centres of mass with respect to the affine assumption.

3. Results and discussion

3.1 Motion of a single fibre: numerical simulation vs. dumbbell approach

The kinematics of a single fibre in a squeezed suspending fluid was first analysed (i) to investigate the influence of the confinement and the rheology of the suspending fluid, (ii) and to check the capability of the analytical dumbbell model to recover simulation results. For that purpose, the simulated fibre was idealised as a sphero-cylinder of length $l + d$ (in accordance with Fig. 3) with an aspect ratio $\beta \approx 15$ close to that measured experimentally

(next subsection). The fibers are put in the reference plane Oxy ($\varphi_{i0} = 0°$.) and the suspending fluid had either a Newtonian ($n = 1$) or a power-law viscosity with high strain-thinning effects ($n = 0.2$). Note that we also performed simulations without confinement, *i.e.,* with $C_0^* = 10$. The corresponding results (not shown here) were identical to those found for the confined situation with $C_0^* = 3$ in section 3.1.1. Lastly, the velocity $\dot{h}$ of the upper plate was arbitrary set to $-100\ \mu m.s^{-1}$: Here again, the trends described in the sequel were identical for other values of $\dot{h}$ (not shown here).

3.1.1 Fibre centered between compression platens

The centre of mass of the fibre was first placed initially at the centre of the fluid domain and computations are made for various initial confinement parameters and angles. Fig. 4 gathers numerical results, dumbbell model and Jeffery's predictions. The Figs. 4(a-b) were built to give rise to large Hencky deformation and fibres were progressively aligned along the plane perpendicular to the compression direction: the initial angles were $\theta_{i0} = 10°$ and $70°$, whereas the initial heights of the sample h_0 were 12 and 4 *mm*, leading to initial confinement parameters $C_0^* = h_0/l$ equal to 3 and 1.3. For Figs. 4(c-f), parameter ranges were chosen close to experimental situations (small strain deformation): the initial angle was $\theta_{i0} = 30°$ and the initial height of the sample h_0 was varied, being equal to 7, 3 and 2.7 mm, leading to initial confinement parameters C_0^* equal to 2.3, 1 and 0.9, respectively.

From these figures, we can deduce the following comments:

- If there is not contact between the fiber and the platens, the evolutions of the out-of-plane angle θ_i plotted in Figs. 4(a, b, e, f) showed that the predictions of the Jeffery's model, *i.e.,* Eq. (2) and the dumbbell model Eq. (19), were very close to the numerical results when a Newtonian fluid was considered. The small differences observed can be related to the aspect ratios of the cylinder used in Jeffery's model which is slightly different from sphero-cylinder used in simulations. Moreover, a small difference of the rotation between Jeffery's and the dumbbell predictions is due to their relative aspect ratios, $\lambda = 0.984$ and 1 respectively. Thus, despite the poor scale separation parameters $C_0^* = \mathcal{O}(1)$, the Jeffery's

model is robust enough for these confined situations. For a highly strain-thinning power-law fluid ($n = 0.2$), the relevance of the Jeffery's and the dumbbell model was still very satisfactory for the same flow configurations. This result is surprising bearing in mind the significant differences reported in the literature when shearing suspensions with other fluids such as viscoelastic fluids [28, 29].

- Secondly, it is also worth noting that fibres also exhibited faster θ-rotations as they touched the compression platens (Fig. 4b, orange arrow, $|\varepsilon_{33}| \sim 0.3$ and , $C_0^* = 1.3$; Figs. 4(c-f), $|\varepsilon_{33}| \sim 0.2$ and , $C_0^* = 1.$ and 0.9) for both Newtonian and highly strain-thinning power-law fluid. These figures also show that (i) this rotation change did not depend on the rheology of the suspending fluid, (ii) the Jeffery's model failed to predict the numerical fibre orientation and (iii) the proposed dumbbell approach Eqs. (23, 25) fairly well predicted them.
- During compression, the simulated orientation angle φ_i remained unchanged and equal to its initial value φ_{i0}, regardless of the values of n and C^*. This is in accordance with the prediction of the standard Jeffery's model and with the dumbbell approach Eqs. (22, 24).
- To check whether the fibre translation followed an affine motion with the macroscale suspension flow (this assumption is embedded in the Jeffery's and the dumbbell models), the numerical deviation $\Delta x_i^{num} = \left\|\mathbf{x}_{G_i}^{num} - \mathbf{x}_{G_i}^{J}\right\| / h_{ref}$ was plotted in Fig. 4d as a function of $|\varepsilon_{33}|$, where $\mathbf{x}_{G_i}^{num}$ is the simulated position of the fibre centre of mass and $\mathbf{x}_{G_i}^{J}$ the position that was predicted using an affine motion with the macroscale velocity gradient (h_{ref} was set equal to $12\,\mathrm{mm}$ to obtain comparable results). The graph proves that the deviation Δx_i^{num} remained small ($< 1\,\%$). However, this deviation is always slightly higher for the power-law fluid than for the Newtonian fluid. Thus, regardless of the investigated power-law index n and and the (non-)occurrence of contacts, it is fair to conclude that for the considered symmetrical configuration, the predicted fibre translation followed the affine assumption that was presumed by the Jeffery's and the dumbbell models.

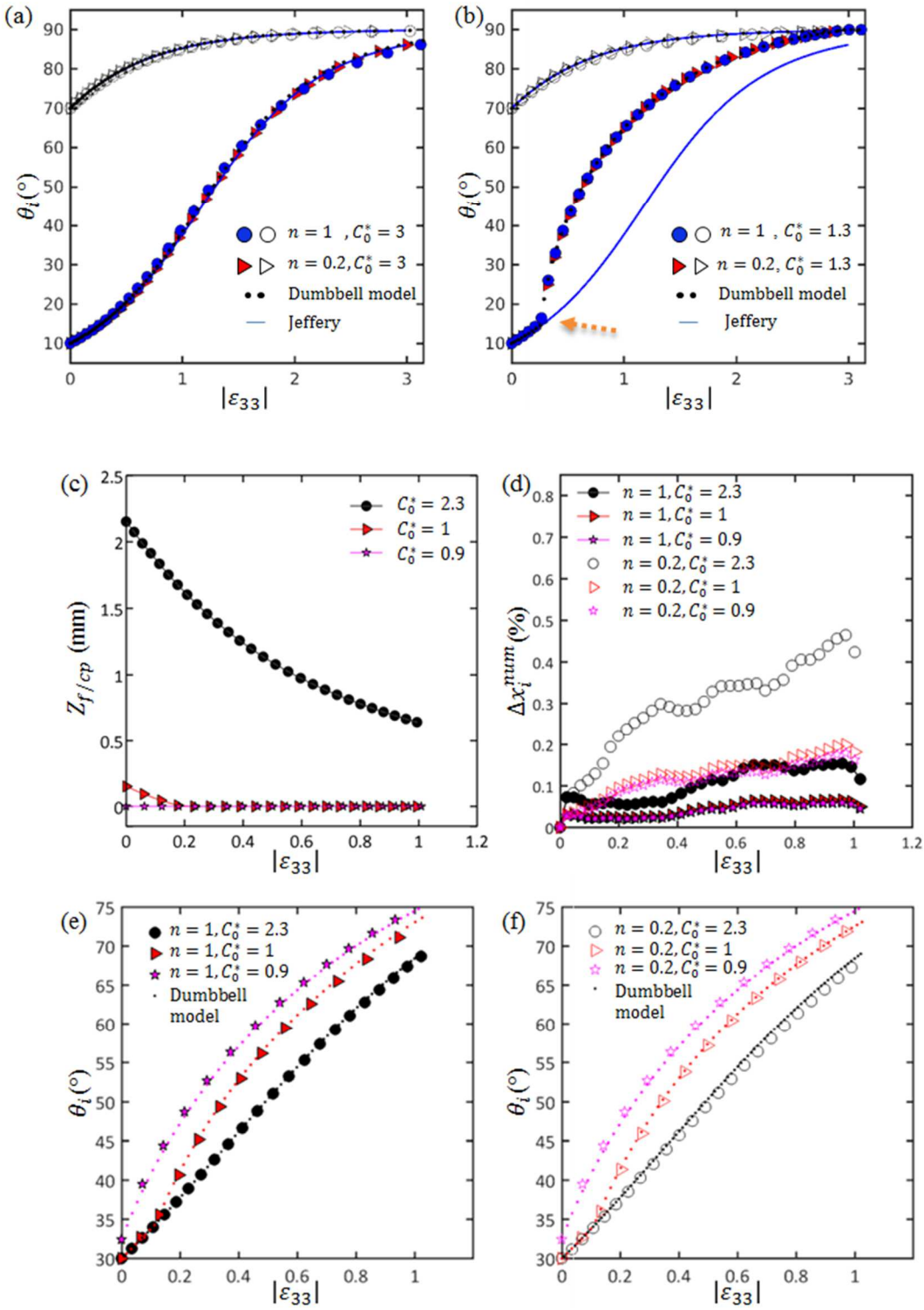

Figure 4. Compression of samples with a centred fibre immersed in Newtonian and power-law fluids ($n = 1$ and 0.2) for different initial confinement parameters: (a) $C_0^* = 3$; (b) $C_0^* = 1.3$ and (c-f) $C_0^* = 2.3; 1; 0.9$. In (a-b) and (e-f), evolutions of the orientation angle θ_i with $|\varepsilon_{33}|$ and comparison between numerical computations (marks) the dumbbell model (dotted line) and Jeffery's predictions (line). The evolutions of the fibre/platens distance $Z_{f/cp}$ and the dispersion Δx_i^{num} with $|\varepsilon_{33}|$ are plotted in (c) and (d), respectively.

3.1.2 Asymmetrical case

The situations where a fibre was initially located nearer to the lower platen were also investigated. For that, an initial sample height $h_0 = 7\,\mathrm{mm}$ $(C_0^* = 2.3)$ was chosen and the fibre was positioned such as one extremity was $0.11\,\mathrm{mm}$ away from the lower platen. The initial orientation was the same as in the previous section. Results are reported in Fig. 5 where simulated and analytical evolutions of the out-of-plane angle θ_i and the dispersion Δx_i^{num} are plotted as function of the compression strain $|\varepsilon_{33}|$.

- Similarly to the symmetrical case, the simulated orientation angle φ_i remained constant (not shown here), regardless of the considered fluid and in accordance with the Jeffery's and dumbbell models.
- For the Newtonian fluid, a good accordance between the Jeffery's predictions and the simulation was also noticed while the fibre did not touch the lower platen, *i.e.*, while $|\varepsilon_{33}| < 0.15$: Jeffery's orbit was well followed by the simulation (Fig. 5a), as well as the affine motion of the centre of mass of the fibre (Fig. 5b). As the compression strains remained moderate before contact, this result was also valid for the strain-thinning fluid.
- After the contact indicated by the dotted arrows, this was no more valid. Firstly, the fibre rotation was faster than that predicted by the Jeffery's model (Fig. 5a), but lower than the rotation recorded for the symmetrical case (Fig 4c-d). Secondly, noticeable deviations of the fibre translation from the affine assumption were observed (Fig. 5b). It is also interesting to notice that these tendencies were practically identical for the Newtonian and the highly strain-thinning fluid. Lastly, the graphs in Fig. 5 show the fairly good predictions of the dumbbell model Eqs. (31-32).

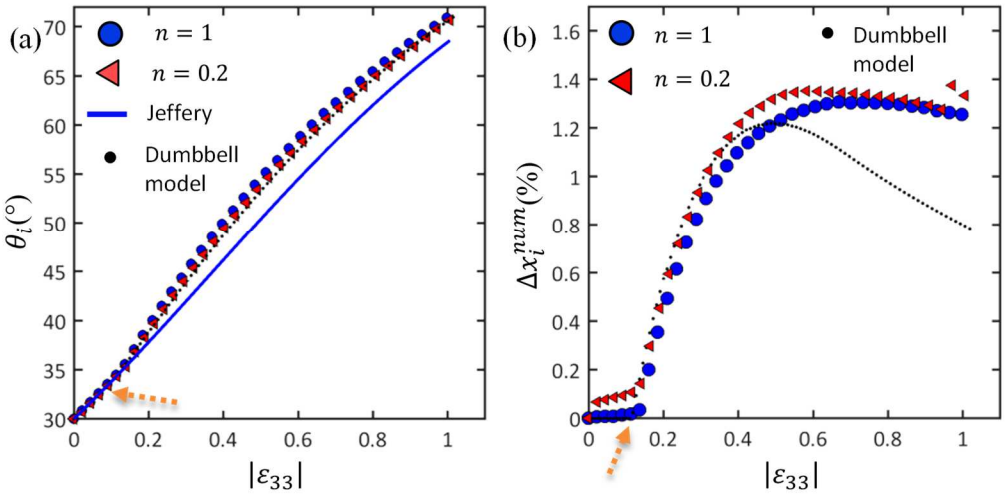

Figure 5. Compression of samples with a non-centred fibre immersed in Newtonian and power-law fluids ($n = 1$ and 0.2) and with $C_0^* = 2.3$. Evolutions of the fibre orientation angle θ_i (left graphs) and the deviation Δx_i^{num} (right graphs) with $|\varepsilon_{33}|$: numerical simulations (marks), predictions of the Jeffery's (line) and the dumbbell (dotted line) models.

3.2 Comparison with experiments

The results of the experiments reported in [43], summarised in subsection 2.3 are now compared with the predictions of the numerical simulations with cylindrical fibres, the Jeffery's and the dumbbell models. As stated in subsection 2.1, the sample sizes, the fibre geometry (with a cylindrical shape), orientations and positions and the punch velocities were used as numerical input data for the simulations. Results are shown in Figs. 6 and 7. Those obtained with the suspensions with one fibre (samples 1 to 6) are gathered in Fig. 6, whereas Fig. 7 refers to dilute fibre suspensions (samples 7 to 9). The graphs a-b in Fig. 6 and a-f in Fig. 7 show the evolutions of the angles θ_i and φ_i of each fibre i with the compression strain $|\varepsilon_{33}|$. Graph (c) in Fig. 6 shows the evolution with $|\varepsilon_{33}|$ of the numerical (resp. experimental) deviations Δx_i^{num} (resp. $\Delta x_i^{exp} = \left\|\mathbf{x}_{G_i}^{exp} - \mathbf{x}_{G_i}^{J}\right\|/h_0$) of the fibre centres of mass (corresponding minimal and maximal values are listed in Tab. 1). The following comments can be made.

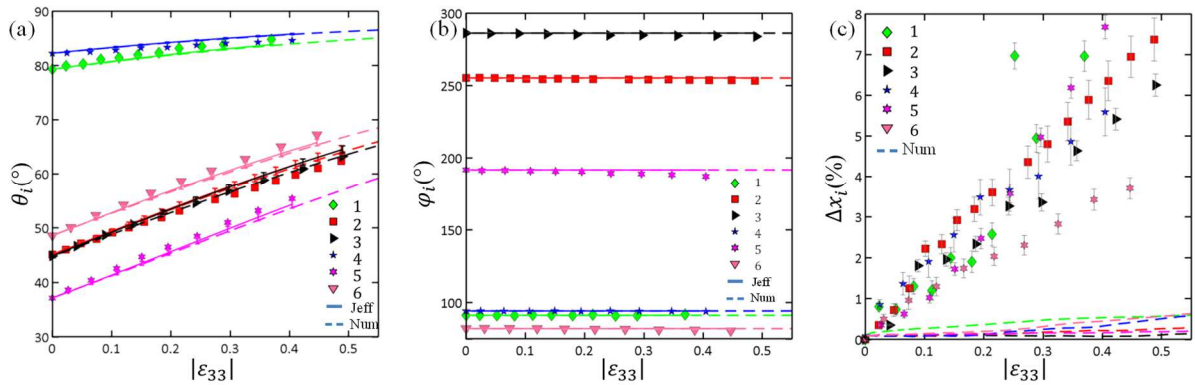

Figure 6. Compression of sample 1 to 6 (one fibre per sample). Evolutions of the measured (marks), analytically (lines, Jeffery's model) and numerically (dashed lines) predicted angles θ_i (a) and φ_i (b) with $|\varepsilon_{33}|$. Experimental and numerical evolutions of the deviations Δx_i^{exp} and Δx_i^{num} with $|\varepsilon_{33}|$.

- For the samples with one fibre, Fig. 6 shows the fairly good accordance between the experimental and simulation results. Indeed, regardless of the considered initial fibre orientations, the simulations well captured, *i.e.*, with a maximal difference of $3°$, both the stagnation of the in-plane angles φ_i and the increase in the out-of-plane angles θ_i during compression. However, the numerical deviations Δx_i^{num} remained close to 0 ($< 0.5\%$), whereas Δx_i^{exp} could reach several percent ($< 8\%$) after experimental compressions (Fig. 6c). As previously mentioned [43], experimental deviations Δx_i^{exp} could probably be attributed to undesirable rigid body motions of the compressed samples that altered these measurements. Thus, despite this discrepancy, results of Fig. 6 tend to validate the numerical approach as a proper method to finely model the kinematics of fibres immersed in non-Newtonian suspending fluids.
- In spite of both the low power law index of the suspending fluid and the flow of the suspensions in narrow gaps ($C^* = \mathcal{O}(1)$), Fig. 6 again shows the robustness and relevance of the Jeffery's model (as well as the dumbbell model). Again the analytical predictions of orientation angles show a good accordance with numerical and experimental results. Note that this remark is valid because fibres considered here did not touch the compression platens.
- For dilute fibre suspensions (samples 7 to 9), the angles θ_i increased during compression while the angles φ_i remained more or less constant (Fig. 7), in a way similar to the

samples with one fibre (Fig. 6). However, for some fibres, as indicated by the arrows in Fig. 7c-f, the angles φ_i slightly varied and the angles θ_i increased more rapidly at given compression strains. As shown in Fig 7, apart from the simulated angles φ_i for the marked fibres shown by the arrows, it is interesting to note that the aforementioned experimental trends were rather well-captured by the numerical simulation.

- Also, Fig. 7 proves that predictions of Jeffery's model are satisfactory, except for the fibres shown by the arrow where the predicted angles θ_i are noticeably lower than the experimental and simulated angles. As the considered concentration regime is dilute, the origins of these discrepancies should not be related to fibre-fibre contacts. Both acquired 3D images and simulation results helped us to check this point. In addition, deviations should not be induced by long range hydrodynamic interactions between fibres. Thanks to the simulation, this assumption could be verified: the generalised shear rate colormaps in Fig. 8 showed that high shear rate zones were located in the vicinity of fibres only, *i.e.,* in zones with a thickness close to one fibre diameter d. This phenomenon should not alter the kinematics of other fibres.
- Note also that for this dilute suspension, the main stress tensor corresponds globally to a squeeze flow and the flow motion remains axisymmetric. In particular a plug flow is always observed.

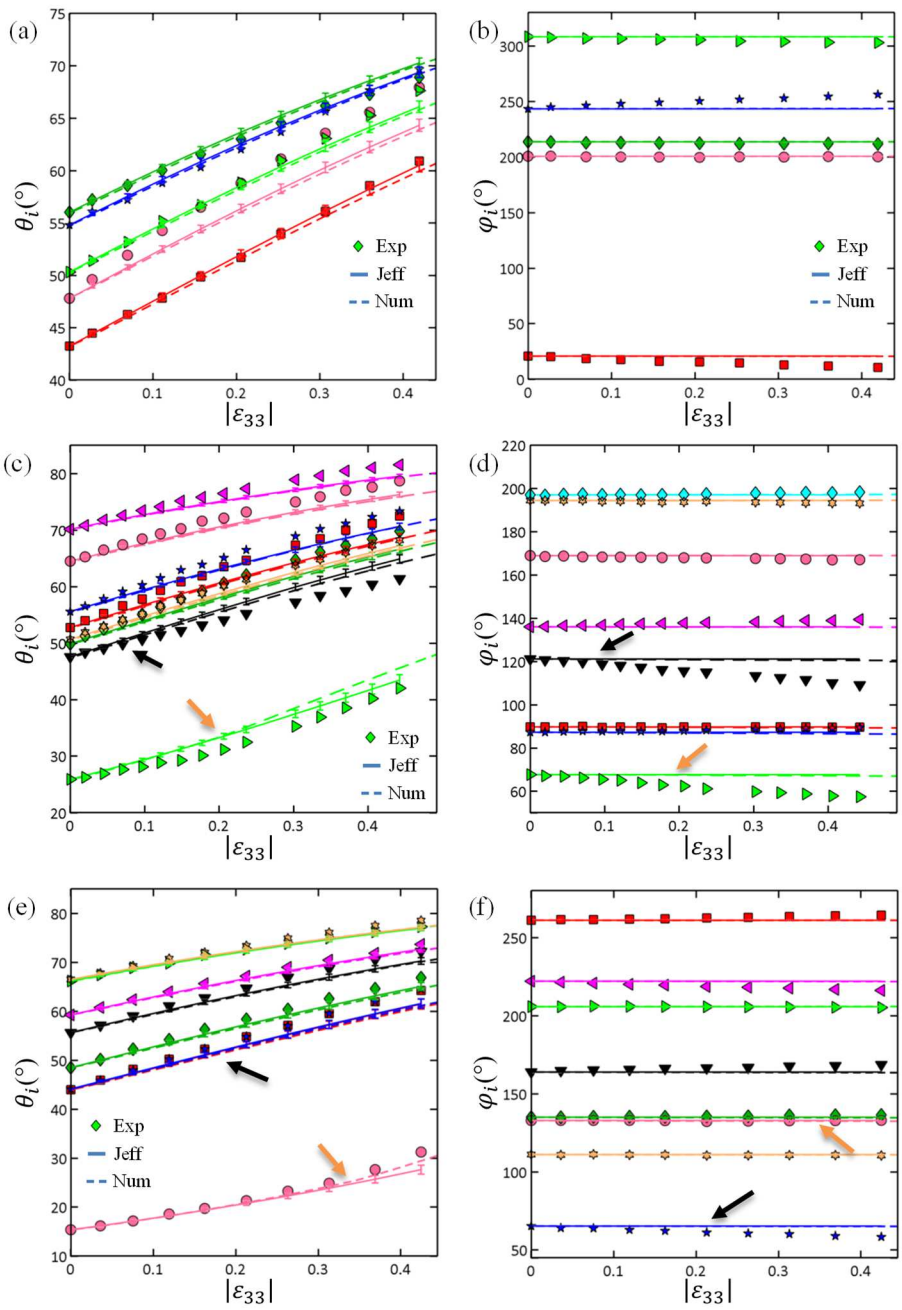

Figure 7. Compression of samples 7 to 9. Evolutions of the measured (marks), analytically (lines, Jeffery's model) and numerically (dashed lines) predicted angles θ_i (a) and φ_i (b) with $|\varepsilon_{33}|$. Black arrows denote fibres closed to the walls (less than half one fibre diameter) whereas orange arrows show the contact with platen(s) during compression.

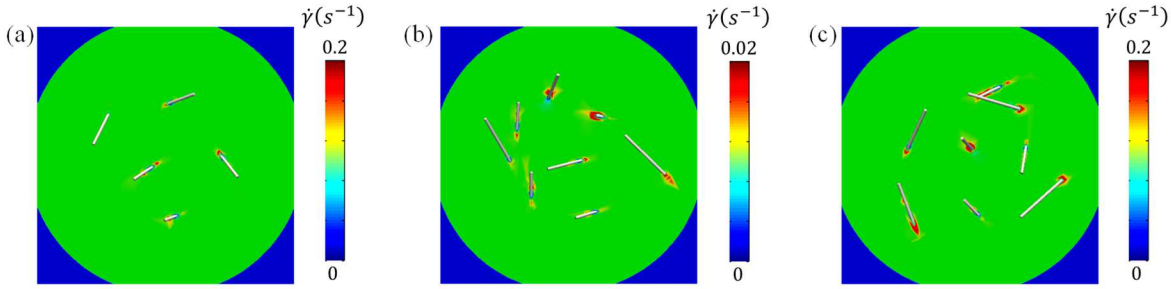

Figure 8. Horizontal slices in the middle of the numerical samples showing colormaps of the generalised shear rate $\dot{\gamma}_{eq}$ at a compression strain $|\varepsilon_{33}| = 0.4$ for samples 7 (a), 8 (b) and 9 (c).

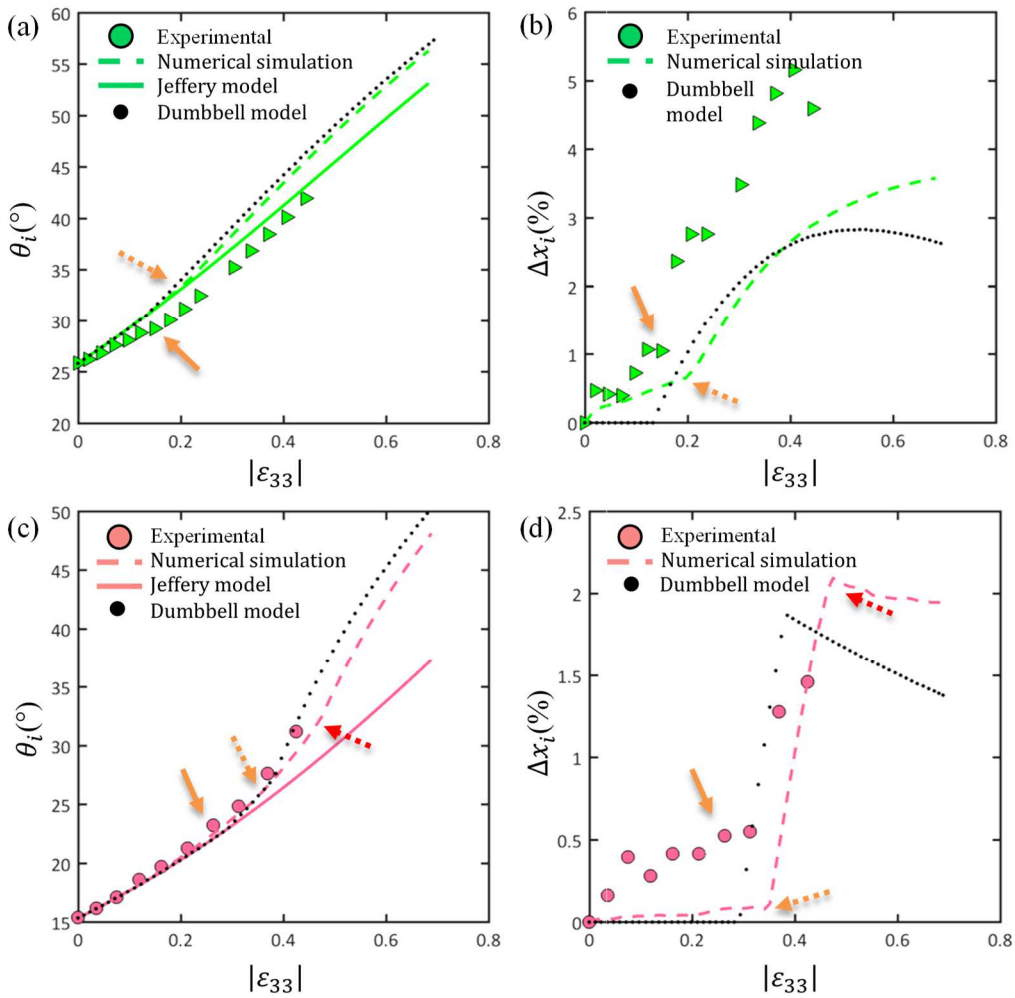

Figure 9. Evolutions of the angles θ_i (a,c) and the deviations Δx_i^{exp} and Δx_i^{num} (b,d) for two fibres in contact with compression platens in samples 8 (a) and 9 (b). The orange arrows (experimental: filled, numerical: dotted) denote the first contact of the considered fibre with the upper platen, and the red arrows the second with the lower platen.

- Thus, the observed and simulated contacts of fibres with platens were probably be the main reason for the observed discrepancies. More precisely, when contacts with the platens occurred, both the numerical fibre orientation and deviation from the affine assumption deviated abnormally away from the Jeffery's prediction. This is shown in Fig.

9 for the kinematics of two fibres, namely those indicated by the green triangles and pink circles in Fig. 7c-d and Fig. 7e-f, respectively. The dotted orange (resp. red) arrows in Fig. 9 denote the occurrence of the numerical contacts between the considered fibre and one (resp. two) compression platen. Fig. 9a-b show that the first contact occurred at $|\varepsilon_{33}| \sim 0.2$, whereas in Fig. 9c-d the fibre extremity firstly entered in contact with the upper platen at $|\varepsilon_{33}| = 0.34$. The numerical description could be improved. Indeed, contacts were detected a bit earlier in the experiments than in the simulations. Simulation results were semi-quantitatively in accordance with the experiments for the deviations Δx_i^{num}**.** However, in this case, experimental artefacts could have altered the values of Δx_i^{exp} (*cf.* the first point above)**.** A discrepancy between experimental and numerical orientation angle θ_i was observed in Fig. 9a. On the contrary, the numerical description of the orientation angle θ_i was very good in Fig. 9c. Lastly, it is worth mentioning that the analytical predictions proposed by the dumbbell model were also acceptable and very close to numerical results. A small difference was obtained between the analytical and numerical results, as the simulated fibres were cylinders (in accordance with the experiments) and not sphero-cylinders (underlying assumption of the present dumbbell model).

4. Concluding remarks

To better understand flow-induced fibrous microstructures in short fibre-reinforced composites during their forming operations, the kinematics of fibres in fibre suspensions were finely investigated. For that purpose, we combined fibre scale FE numerical simulations, analytical modelling and rheometry experiments coupled with 3D real time observations of their evolving fibrous microstructures. Restraining the study to dilute systems, as a first step towards more concentrated regimes, the analysis aimed to answer on three major and open questions. What is the effect of the non-Newtonian rheology of the suspending fluid on the fibre kinematics? What is the effect of confinement? Is there a

relevant compact analytical model to describe these effects? The main conclusions drawn from this study are given hereafter:

- From a methodological standpoint, a monolithic and multiphase Eulerian FE formulation was used. This FE was able to model, using levelsets, transport and advanced meshing algorithms, the motion of rigid fibres immersed in power-law fluids. It was proved that this numerical framework could recover the well-known Jeffery's kinematics of a single fibre in a Newtonian fluid under unconfined and homogeneous compression flow. The FE results were also compared with 3D images obtained previously [43] in the case of confined lubricated compression of power-law strain-thinning suspending fluid containing one or several fibres. The original comparison was rigorously achieved, *i.e.*, using the initial 3D images as initial conditions as well as the experimental boundary conditions measured during compression. The good accordance between simulation and experimental results demonstrated the validity of the FE approach to study at the fibre scale the rheology of dilute fibre suspensions with power law fluids and confined flow situations.
- For the considered flows and fluid rheologies, *i.e.*, lubricated compression with Newtonian or strain-thinning power-law fluids ($n = 0.2$) close to industrial polymer matrices, it was fair to conclude that fibre kinematics was practically not affected by the fluid rheology. It could be interesting to validate this key result for lower values of $n \to 0$, and yield stress or viscoelastic fluids, as well as for other fibre aspect ratios.
- Combining experimental and numerical results, the effects of confinement on fibre kinematics was investigated in detail. Astonishingly, while fibres did not touch walls, *i.e.*, even for low values of the confinement parameter, numerical simulations proved that the fibre kinematics could be considered to be unaffected. Under such circumstances, the rotation of fibres could be described using the Jeffery's equation and the translation of the centres of mass of fibres followed affine motion with the macroscale flow field of the suspensions. Confinement effects arose when fibres touched the compression platens. Then, the affinity of the motion of fibres was lost, and fibres rotation deviated from the

Jeffery's orbit, with a faster rotation rate. These numerical trends were supported by experimental observations.

- From these results, we validated an extension of the dumbbell model [41] as a heuristic alternative of the Jeffery's equations to analytically predict the motion of fibres in the considered flow situations, *i.e.*, for power-law fluids and elongational confined or unconfined flows. Similar results were obtained by using a cell model around a fiber in [59]. For unconfined or confined flows without contact between fibres and walls, the dumbbell model is equivalent to the Jeffery's equations for slender fibres, regardless of the rheology of the considered fluids. This model provides nice fitting of numerical simulations and experiments. When fibres touched the walls, analytical corrections of the Jeffery's equations were found to describe the non-affine translation of contacting fibres and their increasing rotation rate. These corrections did not depend on the fluid rheology, could well capture the observed numerical and experimental trends. They could also be implemented in software used to predict the forming operations of short fibre-reinforced polymer composites.

Acknowledgments

T. Laurencin gratefully acknowledges the LabEx Tec21 (Inv. d'Avenir - grant agreement n°ANR-11-LABX-0030) for his PhD research grant. The 3SR Lab is part of LabEx Tec 21 and the Carnot Institute Polynat.

References

[1] S. Advani, Flow and Rheology in Polymer Composites Manufacturing, vol. 10 of Composite Materials Series. Elsevier, 1994.
[2] M. Djalili-Moghaddam and S. Toll, "Fibre suspension rheology: Effect of concentration, aspect ratio and fibre size," *Rheol. Acta*, vol. 45, pp. 315–320, 2006.
[3] S. Fu and B. Lauke, "Effects of fiber length and fiber orientation distributions on the tensile strength of short-fiber-reinforced polymers," *Composites Science and Technology*, vol. 56, no. 10, pp. 1179–1190, 1996.
[4] H. Diamant, "Hydrodynamic interaction in confined geometries," *J Phys*, vol. 78, 2009.
[5] R. Schiek and E. Shaqfeh, "Oscillatory shear of a confined fiber suspension," *J Rheol*, vol. 41, pp. 445-466, 1997.
[6] B. Snook, E. Guazzelli, and J. Butler, "Vorticity alignment of rigid fibers in an oscillatory shear flow: Role of confinement," *Phys Fluids*, vol. 24, p. 121702, 2012.
[7] G. B. Jeffery, "The motion of ellipsoidal particles immersed in a viscous fluid," *Proc. Roy. Soc. London*, vol. (A) 102, pp. 161–179, 1922.
[8] H. Brenner, "Rheology of a dilute suspension of axisymmetric brownian particles," *Int. J. Multiphase Flow*, vol. 1, pp. 195–341, 1974.
[9] A. Binder, "The motion of cylindrical particles in viscous flow," *J Appl Phys*, vol. 10, p. 711, 1939.
[10] M. P. Petrich, D. L. Koch, and C. Cohen, "An experimental determination of the stress-microstructure relationship in semi-concentrated fiber suspensions," *J Non-Newtonian Fluid Mech*, vol. 95, pp. 101–133, 2000.
[11] G. Taylor, "The motion of ellipsoidal particles in a viscous fluid", *Proc. R. Soc. London*, vol. A103, pp. 58–61, 1923.
[12] B. J. Trevelyan and S. G. Mason, "Particle motions in sheared suspensions I. rotations," *J. Colloid Sci.*, vol. 6, pp. 354–367, 1951.
[13] E. Anczurowski and S. G. Mason, "Particle motions in sheared suspensions XXIV. rotation of rigid spheroids ans cylinders," *Trans. Soc. Rheol.*, vol. 12, p. 209, 1968.
[14] M. Rahnama, D. L. Koch, and C. Cohen, "Observations of fiber orientation in suspensions subjected to planar extensional flows," *Phys. Fluids*, vol. 7 (8), pp. 1811–1817, 1995.
[15] S. Sinha-Ray, K. Fezzaa, and A. L. Yarin, "The internal structure of suspensions in uniaxial elongation," *J Appl. Phys.*, vol. 113, 2013.
[16] R. S. Bay, Fiber Orientation in Injection Molded Composites : A Comparison of Theory End Experiments. PhD thesis, University of Illinois, USA, 1991.
[17] F. Folgar and C. L. Tucker, "Orientation behavior of fibers in concentrated suspensions," *J Reinf Plast Compos*, vol. 3, pp. 98–118, 1984.
[18] D. L. Koch, "A model for orientational diffusion in fiber suspensions," *Phys Fluids*, vol. 7 (8), pp. 2086–2088, 1995.
[19] N. Phan-Thien, X. J. Fan, R. I. Tanner, and R. Zheng, "Folgar-tucker constant for a fibre suspension in a newtonian fluid," *J. Non-Newtonian Fluid Mech.*, vol. 103, pp. 251–260, 2002.
[20] J. Phelps and C. Tucker, "An anisotropic rotary diffusion model for fiber orientation in short- and long-fiber thermoplastics," *J. Non-Newtonian Fluid Mech.*, vol. 156, pp. 165–176, 2009.
[21] P. Dumont, J.-P. Vassal, L. Orgéas, V. Michaud, D. Favier, and J.-E. Månson, "Processing, characterization and rheology of transparent concentrated fibre bundle suspensions," *Rheol Acta*, vol. 46, pp. 639–651, 2007.
[22] P. J. J. Dumont, S. Le Corre, L. Orgéas, and D. Favier, "A numerical analysis of the evolution of bundle orientation in concentrated fibre-bundle suspensions," *J. Non-Newtonian Fluid Mech.*, vol. 160, pp. 76–92, 2009.
[23] T. H. Le, P. J. J. Dumont, L. Orgéas, D. Favier, L. Salvo, and E. Boller, "X-ray phase contrast microtomography for the analysis of the fibrous microstructure of SMC composites," *Compos Part A*, vol. 39, pp. 91–103, 2008.
[24] E. Bartram, H. L. Golflsmith, and S. G. Mason, "Particle motions in non-newtonian media Ili. further observations in elasücoviscous fluids," *Rheol Acta*, vol. 14, pp. 776–782, 1975.

[25] G. D'Avino, P. Maffettone, M. Hulsen, and G. Peters, "A numerical method for simulating concentrated rigid particle suspensions in an elongational flow using a fixed grid," *J. Computational Physics*, vol. 226, pp. 688–711, 2007.
[26] G. D'Avino, P. Maffettone, M. Hulsen, and G. Peters, "Numerical simulation of planar elongational flow of concentrated rigid particle suspensions in a viscoelastic fluid," *J. Non-Newtonian Fluid Mech.*, vol. 150, pp. 65–79, 2008.
[27] D. Gunes, R. Scirocco, J. Mewis, and J. Vermant, "Flow-induced orientation of non-spherical particles: Effect of aspect ratio and medium rheology," *J. Non-Newtonian Fluid Mech.*, vol. 155, pp. 39–50, 2008.
[28] Y. Iso, C. Cohen, and D. L. Koch, "Orientation in simple shear flow of semi-dilute fiber suspensions. 2. highly elastic fluids," *J. Non-Newtonian Fluid Mech.*, vol. 62, pp. 135–153, 1996.
[29] Y. Iso, D. L. Koch, and C. Cohen, "Orientation in simple shear flow of semi-dilute fiber suspensions. 1. weakly elastic fluids," *J. Non-Newtonian Fluid Mech.*, vol. 62, pp. 115–134, 1996.
[30] S. J. Johnson, A. J. Salem, and G. G. Fuller, "Dynamics of colloidal particles in sheared, non-newtonian fluids," *J. Non-Newtonian Fluid Mech.*, vol. 89, pp. 89–121, 1990.
[31] L. G. Leal, "The slow motion of slender rod-like particles in a second-order fluid," *J Fluid Mech*, vol. 69, pp. 305–337, 1975.
[32] P. Brunn, "The slow motion of a rigid particle in a second-order fluid," *J Fluid Mech*, vol. 82, pp. 529–547, 1977.
[33] D. Borzacchiello, E. Abisset-Chavanne, F. Chinesta, and R. Keunings, "Orientation kinematics of short fibres in a second-order viscoelastic fluid," *Rheol Acta*, vol. 55, pp. 397–409, 2016.
[34] G. D'Avino, M.A. Hulsen, F. Greco and P.L. Maffettone, "Bistability and metabistability scenario in the dynamics of an ellipsoidal particle in a sheared viscoelastic fluid," *Phys Rev E*, vol. 89, 2014.
[35] A. Carlsson, F. Lundell, and D. Soderberg, "The wall effect on the orientation of fibres in a shear flow," in *Annual transactions of the nordic rheology society*, 2006.
[36] R. Holm, "Shear influence on fibre orientation," *Rheol Acta*, vol. 46, pp. 721–729, 2007.
[37] K. Moses, S. Advani, and A. Reinhardt, "Investigation of fiber motion near solid boundaries in simple shear flow," *Rheol Acta*, vol. 40, pp. 296–306, 2001.
[38] W. Russel and E. Hinch, "Rods falling near a vertical wall," *J Fluid Mech*, vol. 83, pp. 273–287, 1977.
[39] C. Stover and C.Cohen, "The motion of rodlike particles in the pressure driven flow between two plates," *Rheol Acta*, vol. 29, pp. 192–203, 1990.
[40] A. Ozolins and U. Strautins, "Simple models for wall effect in fiber suspension flows," *Mathematical Modelling and Analysis*, vol. 19, pp. 75–84, 2014.
[41] M. Perez, A. Scheuer, E. Abisset-Chavanne, F. Chinesta, and R. Keunings, "A multi-scale description of orientation in simple shear flows of confined rod suspensions," *J. Non-newtonian Fluid Mech.*, vol. 233, pp. 61–74, 2016.
[42] A. Scheuer, E. Abisset-Chavanne, F. Chinesta, and R. Keunings, "Second gradient modelling of orientation development and rheology of dilute confined suspension," *J. Non-newtonian Fluid Mech.*, vol. 237, pp. 54–64, 2016.
[43] T. Laurencin, L. Orgéas, P. Dumont, S. R. du Roscoat, P. Laure, S. L. Corre, L. Silva, R. Mokso, and Terrien, "3d real-time and in situ characterisation of fibre kinematics in dilute non-newtonian fibre suspensions during confined and lubricated compression flow," *Composites Science Technology*, vol. 134, pp. 258–266, 2016.
[44] R. Bird, R. Armstrong, and O. Hassager, Dynamics of Polymeric Liquids,Volume 1: Fluid Mechanics 2nd Edition. Wiley, 1987.
[45] C. Binetruy, F. Chinesta, and R. Keunings, *Flows in Polymers, Reinforced Polymers and Composites: A multi-scale Approach*, ch. Complex Flows of Micro/Nano Structured Fluids: Reinforced Polymer Composites, pp. 43–108. Springer International Publishing, 2015.
[46] T. Coupez, H. Digonnet, E. Hachem, P. Laure, L. Silva, and R. Valette, Multidomain Finite Element Computations: Application to Multiphasic Problems, Arbitrary Lagrangian-Eulerian and Fluid-Structure Interaction. Numerical Simulation. Wiley, 2010.
[47] T. Laurencin, Etude de la rhéologie des suspensions de fibres non-Newtoniennes par imagerie et simulation numérique 3D à l'échelle des fibres. PhD thesis, Université Grenoble-Alpes, 2017.
[48] S. Osher and J. Sethian, "Front propagating with curvature-dependent speed. algorithm based on hamilton-jacobi formulations," *J. Comput. Phys.*, vol. 79, pp. 12–49, 1988.
[49] M. Fortin and R. Glowinski, Augmented Lagrangian Methods, Applications to the Numerical Solution of Boundary-Value Problems. North Holland, 1983.
[50] E. Pichelin and T. Coupez, "Finite element solution of 3d mold filling problem for viscous incompressible fluid," *Comput. Methods Appl. Mech. Engrg*, vol. 163, pp. 359–371, 1998.

[51] H. Digonnet, T. Coupez, P. Laure, and L. Silva, “Massively parallel anisotropic mesh adaptation,” The international journal of high performance computing applications, //doi.org/10.1177/1094342017693906, 2017.
[52] L. Ville, L. Silva, and T. Coupez, “Convected level set method for the numerical simulation of fluid buckling”, *Int. J. Numer. Meth. Fluids*, vol. 66, pp. 324–344, 2011.
[53] T. Coupez, “Metric construction by length distribution tensor and edge based error for anisotropic adaptive mesmesh.,” *J. Comp. Phys.*, vol. 230, pp. 2391–20405, 2011.
[54] M. V. Bruschke and S. G. Advani, “Flow of generalized newtonian fluid across a periodic array of cylinders”, *J Rheol*, vol. 37, no. 3, pp. 479–498, 1993.
[55] P. D. M. Spelt, T. Selerland, C. J. Lawrence, and P. D. Lee, “Flows of inelastic non-newtonian fluids through arrays of aligned cylinders. part 1. creeping flows,” *J. Eng. Math.*, vol. 51, pp. 57–80, 2005.
[56] L. Orgéas, C. Geindreau, J.-L. Auriault, and J.-F. Bloch, “Upscaling the flow of generalised newtonian fluids through anisotropic porous media,” *J Non-Newtonian Fluid Mech*, vol. 145, pp. 15–29, 2007.
[57] M.A. Bibbo, S.M. Dinh and R.C. Armstrong,”Shear Flow Properties of Semiconcentrated Fiber Suspensions”, *J Rheol*, 29, pp. 905-929, 1985
[58] J. Wang, W. Yu, C. Zhou,Y. Guo, W. Zoetelief and P. Steeman, “Elongational rheology of glass fiber-filled polymer composites”, Rheol Acta, 55, pp. 833-845, 2016
[59] J. Férec, E. Bertvas, B.C. Khoo, G. Ausias and N. Phan-Thien, “The effect of shear-thinning behaviour on rod orientation in filled fluids”, J. Fluid Mech. 798, pp. 350-370 (2016)